INSTITUTE OF PHYSICS PUBLISHING JOURNAL OF PHYSICS: CONDENSED MATTER

J. Phys.: Condens. Matter **13** (2001) 10561–10576 PII: S0953-8984(01)27041-6

Exploiting the photoelectron source wave with near-node photoelectron holography

Thomas Greber

Physik Institut der Universität Zürich, Winterthurerstrasse 190, CH-8057 Zürich, Switzerland

Received 20 July 2001
Published 9 November 2001
Online at stacks.iop.org/JPhysCM/13/10561

Abstract

Photoelectron diffraction patterns of a large portion of the 2π solid angle above a surface may be used for direct structure determination schemes such as holography. It is shown that the particular experimental set-up of near-node photoelectron holography greatly improves the quality of holographically obtained three-dimensional images of atomic arrangements. In the near-node set-up the diffraction patterns are recorded at an emission angle near the node of a photoelectron source wave and forward scattering is suppressed. 24 distinct atomic sites were observed for the test case of Al 2s ($E_{kin} = 952$ eV) diffraction from Al(111). The physics of photoelectron source waves is recapitulated and the holographic inversion procedure that is based on the multipole expansion is outlined.

(Some figures in this article are in colour only in the electronic version)

1. Introduction

Angle-scanned Auger electron and x-ray photoelectron diffraction (AED, XPD) significantly progressed when the diffraction patterns were measured *and* displayed as 2π-scans, i.e. for all emission directions above the surface [1]. The first substrate XPD 2π-scan was presented by Baird *et al* [2] but for the next decade only a few papers with the same approach appeared [3, 4]. Fully automated angle-scanning experiments by Frank *et al* [5], Seelmann-Eggebert and Richter [6] and Osterwalder *et al* [1] finally demonstrated the usefulness of such data acquisitions and representations: for electron kinetic energies above 500 eV they allow an immediate interpretation of the intensity distributions as forward-scattering features, i.e. as two-dimensional projections of nuclear charge around the emitter. In figure 1 an XPD 2π-scan for Rh(111) is shown in stereographic projection. The intensity of the Rh $3d_{5/2}$ core level is displayed on a linear greyscale, where white indicates the maximum intensity. For the electron kinetic energy of 947 eV which corresponds to an electron wavelength of 0.4 Å, the diffraction pattern is dominated by forward scattering. For the case of Rh with fcc structure it is most prominent along the ⟨110⟩-like densely packed atomic chains at a polar angle of

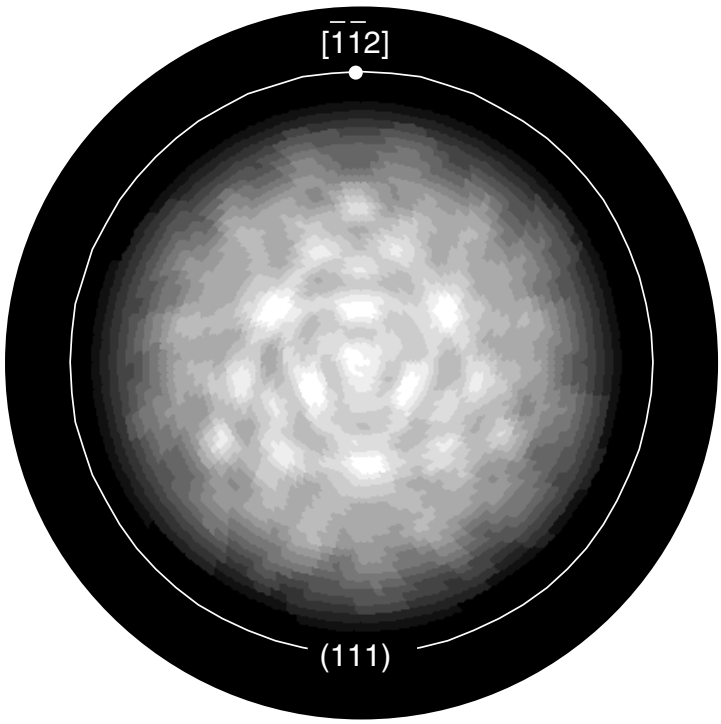

Figure 1. An XPD 2π-scan of Rh(111) in stereographic projection. The intensity of the Rh $3d_{5/2}$ core level ($E_{kin} = 947$ eV) is displayed on a linear greyscale. Data from reference [7].

35.3°. Harp, Saldin and Tonner were the first to interpret such experimental 2π-scans as holograms [8]. It became clear, however, that data of the kind shown in figure 1 are more reliable for interpretation as two-dimensional projections of atoms.

Holography as proposed by Gabor [9] is a solution of the phase problem in diffraction experiments. In structure determination it will keep its prominent role at least for the first guess before other phase-recovery algorithms, as e.g. discussed in this Special Issue in the contributions of Marks, Saldin and Tong, are applied. The success of holographic inversions, i.e. reconstruction of three-dimensional structures, relies on the quality of the diffraction intensity maps (holograms) which should carry a maximum of the necessary phase information. In this article the 'near-node photoelectron holography' approach [10] is outlined. It is a kind of 'inside-source' holography [11] where the experimental geometry for the recording of the holograms is optimized in the sense that one single coherent reference wave is used on routes where disturbing effects like zero-order diffraction or multiple scattering are minimized.

Szöke's concept for 'inside-source' holography [11] (see figure 2) proposes that x-rays or electrons which are created at atomic sites form a hologram in Gabor's sense [9]. After the emission process, the 'coherent beam' splits into an unscattered reference wave Ψ_r and a scattered object wave Ψ_o that interfere in the detector. The measured intensity $I(\boldsymbol{k})$ can thus be written as

$$I(\boldsymbol{k}) = |\Psi_r + \Psi_o|^2 = \Psi_r \Psi_r^\star + \Psi_r \Psi_o^\star + \Psi_o \Psi_r^\star + \Psi_o \Psi_o^\star \tag{1}$$

where $\boldsymbol{k}$ is the wave vector of the reference and the object waves. The intensities of a large

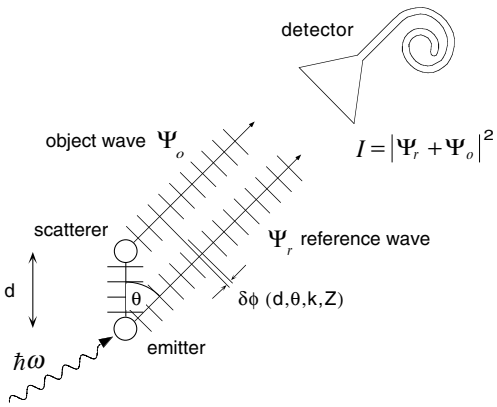

Figure 2. The principle of photoelectron holography as proposed by Szöke [11]. The path-length difference between the unscattered reference wave Ψ_r and the scattered object wave Ψ_o leads to interference. The phase shift $\delta\phi(d, \theta, k, Z)$ between Ψ_r and Ψ_o is a function of the distance d between the emitter and the scatterer, the scattering angle θ, the wave vector k and the scatterer potential which is given by its nuclear charge Z. The intensity distribution $I(\boldsymbol{k}) = |\Psi_r + \Psi_o|^2$ in a large portion of $\boldsymbol{k}$-space is a hologram. From this hologram and the knowledge of the reference wave Ψ_r, the object wave Ψ_o in the near field of the emitter may be reconstructed.

set of $\boldsymbol{k}$-vectors constitute a hologram and permit the reconstruction of an image $U(\boldsymbol{r})$ which maps the surrounding of the emitter in real space. This is realized by the Helmholtz–Kirchhoff theorem which reconstructs the near field around the emitter from its far field $I(\boldsymbol{k})$ [12]. The object wave Ψ_o contains a single-scattering and a multiple-scattering term: $\Psi_o = \Psi_{ss} + \Psi_{ms}$. The $\Psi_r\Psi_{ss}^\star + \Psi_{ss}\Psi_r^\star$ terms contain the information on the spatial arrangement of the object. If the multiple-scattering term Ψ_{ms} is small compared to the single-scattering term Ψ_{ss}, $\Psi_r\Psi_r^\star$ is known and the object self-interference term $\Psi_o\Psi_o^\star$ is small, then $U(\boldsymbol{r})$ is determined by the Fourier transform of $I(\boldsymbol{k})$, i.e. from the interference terms $\Psi_r\Psi_o^\star + \Psi_o\Psi_r^\star$. These interference terms contain an image and a twin image, and methods exist to distinguish between the two [13]. For three-dimensional images, the $\boldsymbol{k}$-space sample has to span three dimensions. This is achieved by scanning two emission angles (see figure 1) and/or $|\boldsymbol{k}|$ (multiple-energy sampling).

Inside-source holography with x-rays [14] and its time-reversed sister with γ-rays [15] have been demonstrated. These kinds of holography apply for heavy elements as scatterers and emitters and for a probed volume which is fairly large. Inside-source holography with electrons is more sensitive, in particular to light elements, and applications with particular emitter geometries have been reported [16]. However, several problems are encountered: in the relevant electron kinetic energy range, the scattering cross section of electrons is of the order of 1 Å^2 and highly anisotropic. The dominant feature of this anisotropy is forward scattering, which is a consequence of the focusing by the attractive ion cores of an incoming electron wave along its $\boldsymbol{k}$-vector [17]. Forward scattering hinders holography because it is a zero-order diffraction feature that contains no information on the path-length differences between the scattered and the unscattered waves.

The anisotropy of a photoelectron source wave, however, may be used in order to suppress forward scattering [10,18]. If the photoelectron intensity is measured at an angle close to a node of a photoelectron p wave, the corresponding photoelectron diffractograms may be interpreted as holograms and the holographic reconstruction yields three-dimensional pictures with a high quality.

Section 2 is a tutorial on photoelectron source waves and its manifestations in experiments are discussed. In section 3 the concept of near-node photoelectron holography and the first proof-of-principle experiments are reviewed. In the appendix the multipole expansion for 2π-scans and its implementation for holographic reconstructions are outlined.

2. The source wave in photoelectron diffraction

The interaction of a photon with an atom breaks its spherical symmetry. If the photon energy exceeds the binding energy of a particular electron level a photoelectron may be emitted. This photoelectron is described as a spherical wave which propagates away from the point where the photoelectron hole was created. The photoemission process is very localized in space and time and provides a perfectly coherent point-source wave. For a 1 keV photoelectron ($\lambda = 0.4$ Å) with lifetime broadening of e.g. 100 meV, this translates into a coherence length ($\ell_c = \lambda^2/\Delta\lambda$) of 0.7 μm. This shows that for all practical purposes the coherence length of the source wave is not a limiting factor. In solids it is rather the inelastic mean free path that limits the volume that is probed by such electron waves. It is of the order of 15 Å and increases above 200 eV roughly $\propto\sqrt{E}$ where E is the kinetic energy of the electrons. In general a photoelectron source wave is not isotropic. This is in contrast to e.g. the case for an Auger electron, where isotropic electron emission is expected as long as spherically symmetric electron shells are involved in the Auger transition [19]. The anisotropy of the photoelectron source wave may be exploited if the direction and polarization of the light are controlled. In photoelectron diffraction this is e.g. used to selectively enhance the sensitivity of the method (see section 2.2).

2.1. The dipole selection rules

The angular momentum character of the photoelectron final state is determined from the dipole selection rules. In non-relativistic notation we find

$$\ell_f = \ell_i \pm 1 \qquad \ell \geqslant 0 \tag{2}$$

where $\hbar\ell_f$ and $\hbar\ell_i$ are the angular momenta of the final and the initial state. For the magnetic quantum number m ($|m| \leqslant \ell$) we find, with the quantization axis along the direction of photon propagation,

$$m_f = m_i \tag{3}$$

for linearly polarized light and

$$m_f = m_i \pm 1 \tag{4}$$

for right or left circularly polarized light, respectively.

For convenience we use in the following $\ell = \ell_i$ and $m = m_f$. The individual $2\ell + 1$ magnetic subshell transitions add incoherently, while the $\ell + 1$ and $\ell - 1$ final states interfere for the $2\ell - 1$ magnetic subshell transitions with $\ell + 1$ *and* $\ell - 1$ contributions. The mixing is determined by the radial matrix elements $R_{\ell-1,m}$ and $R_{\ell+1,m}$ whose phases are shifted by the continuum orbital phase shift $\delta_{\ell\pm1}$ [20].

For $kr \ll \ell$ we get the source wave as

$$\Psi_{source} \propto \frac{e^{ikr}}{r}(R_{\ell+1,m}Y_{\ell+1,m}(\theta,\phi) + R_{\ell-1,m}Y_{\ell-1,m}(\theta,\phi)) \tag{5}$$

where $Y_{\ell m}$ are spherical harmonics. For the simplest case, i.e. the excitation of an s level, $R_{\ell-1,m}$ does not exist and we get a pure p wave with a node along the propagation direction of the light. This is true as long as no relativistic effects come into play [21]. In figure 3 the situation

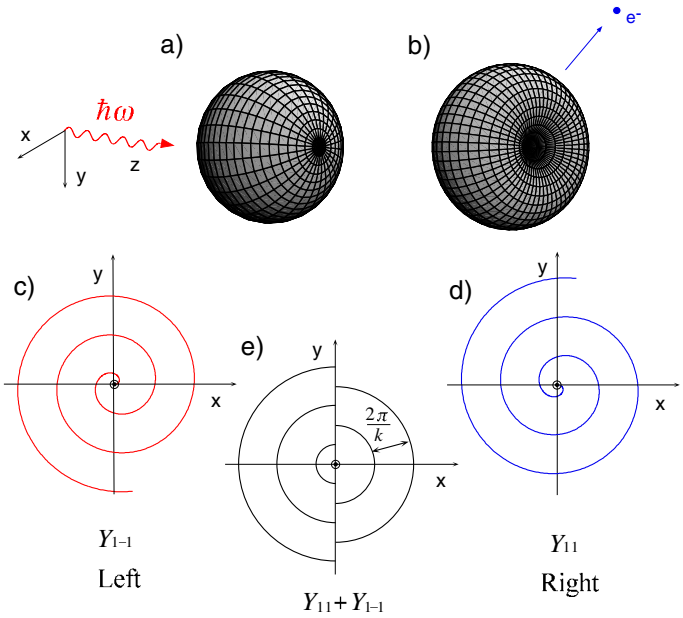

Figure 3. Visualization of a photoelectron wave as excited from an atomic s level. The spherically symmetric s level in (a) is excited by a photon which produces a light-polarization-dependent p source wave ($Y_{11} + \exp(i\varphi)Y_{1-1}$) (b). Note the creation of a node along the direction of propagation of the light. In (c)–(e) the constant-phase planes (wave hills) of the photoelectron wave for left, right and x-polarized light are shown. Classical electron trajectories are orthogonal to these phase planes.

is illustrated. For circularly polarized light the angular momentum of the photoelectron promotes the photoelectrons on handed spiral trajectories while linearly polarized light ejects the electrons preferentially along the direction of the polarization vector $\boldsymbol{A}$.

For a closed shell the angular dependence of the photoemission intensity for linearly polarized light is given by

$$\frac{\mathrm{d}\sigma_{n\ell}}{\mathrm{d}\Omega} = \frac{\sigma_{n\ell}}{4\pi}(1 + \beta_{n\ell} P_2(\cos\gamma)) \tag{6}$$

where $\sigma_{n\ell}$ is the total photoemission cross section and $\beta_{n\ell}$ the asymmetry parameter; these depend on the energy of the photoelectron and the angular momentum of the initial state [22]. $P_2(\cos\gamma)$ is the second Legendre polynomial $\frac{1}{2}(3\cos^2\gamma - 1)$ and γ is the angle between the light polarization vector $\boldsymbol{A}$ and the detector. The asymmetry parameters $\beta_{n\ell}$ describe the branching in the $\ell + 1$ and the $\ell - 1$ channel and were e.g. tabulated by Yeh and Lindau [22]. Far above the ionization threshold the radial matrix element $R_{\ell+1}$ tends to be larger than $R_{\ell-1}$. For $|R_{\ell+1}/R_{\ell-1}| \gg 1$ we get $\beta_\ell = (\ell + 2)/(2\ell + 1)$. For the emission from an s level, a pure p wave is excited and $\beta_{\ell=0} \equiv 2$ follows. This means that the source wave from an s level has a node. As is shown in section 3, the existence of such a node may be used to switch off forward scattering [18].

2.2. Experimental findings

The electron source wave strongly affects angle-scanned electron diffraction patterns. This may e.g. be used for the experimental determination of the source-wave character (ℓ, m), as

was e.g. done for Al LVV Auger transitions [19]. In figure 4 experimental electron diffraction 2π-scans are compared with single-scattering calculations that take the angular momentum character of the electron source wave into account. It is seen that the crystal acts as a filter which produces distinct diffraction patterns for different source waves. The differences in the diffraction patterns in figure 4 cannot be explained by the different electron wavelengths (energies) alone. The fact that the wavefronts of source waves with different m impinge under different angles on a scatterer strongly affects the diffraction patterns. The influence of the source wave is particularly strong at low electron energies [23, 24]. It has to be noted that such effects do occur also for isotropic emissions like in an Auger decay [19], since the diffraction pattern of an isotropic source with ℓ-character depends on the $2\ell + 1$ individual source waves which contribute incoherently to the diffraction pattern.

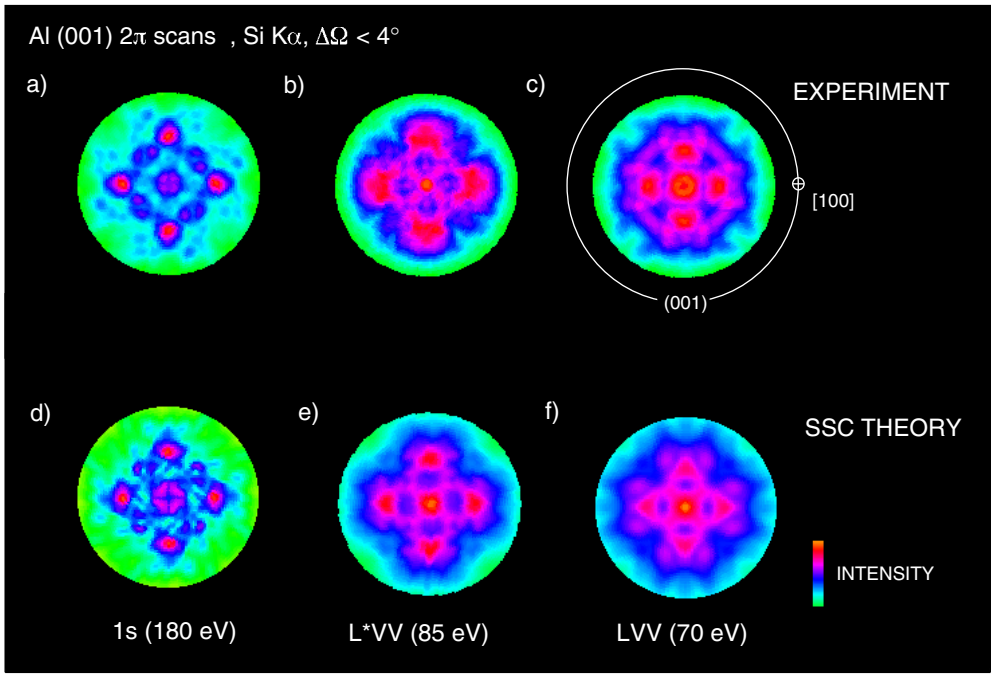

Figure 4. Stereographically projected experimental and theoretical maps of photoelectron and Auger electron emission intensities above an Al(001) surface for Al 1s ($E_{kin} = 180$ eV), Al L*VV ($E_{kin} = 85$ eV) and Al LVV ($E_{kin} = 70$ eV) transitions. The single-scattering cluster calculations take the angular momentum character into account. For the photoemission p-wave final states in the correct light incidence geometry and for the Auger emission, incoherent isotropic s, p, d waves with best-fit weights of 0.08, 0.67, 0.25 for L*VV and 0.24, 0.26, 0.50 for LVV were used. From reference [19].

The angle of incidence and the polarization dependence of the photoelectron source wave, i.e. its anisotropic nature, may be exploited for structure determination. Experiments that investigated the influence of the light polarization on XPD patterns date back to 1984 when Sinković *et al* examined the difference between s- and p-polarized light on the S 1s diffraction patterns in the c(2 × 2)S/Ni(001) system at grazing electron emission angles [25]. Daimon *et al* demonstrated that the position of a forward-scattering peak depends on the source wave. In figure 5 their photoelectron diffraction data with right or left circularly polarized light from Si(001) are shown. Clearly, an angular splitting of the Si 2p forward-scattering peaks is

observed [26]. This splitting and the knowledge of the angular momentum difference of the photoelectrons bears the potential for allowing the determination of the distance between the emitter and the scatterer. Only recently has this idea been further developed into a new method of stereoscopic microscopy for the investigation of atomic arrangements [27].

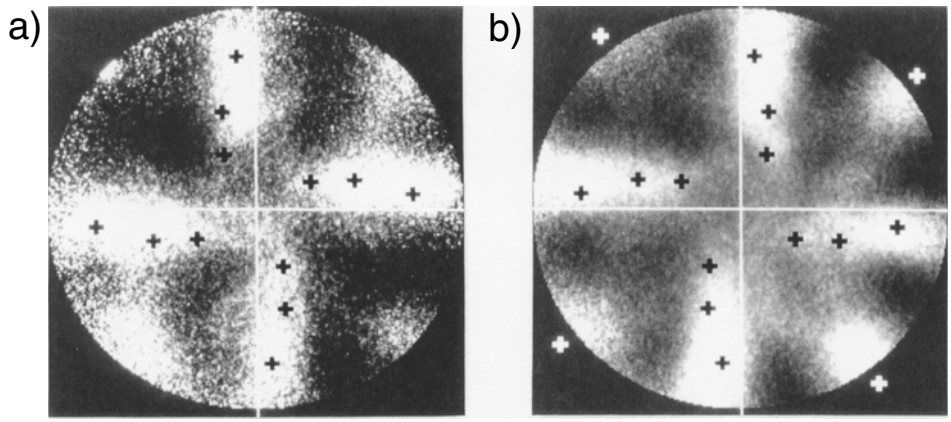

Figure 5. Si 2p photoelectron diffraction patterns from Si(001) with a fixed azimuthal orientation. The electron kinetic energy is 250 eV. Photoemission by (a) left and (b) right circularly polarized light. The crosses mark calculated forward-focusing peaks. Clearly the rotations of the patterns due to the different photon angular momenta can be seen. From reference [26].

The source waves act as directed searchlights which illuminate the object selectively. This was e.g. applied by Sambi and Granozzi in order to get a better sensitivity with respect to the determination of the layer relaxation [28]. A light incidence geometry where the photon's $\boldsymbol{A}$-vector points nearly in the electron's exit direction was used by Li and Tong in order to enhance the surface signal for electron emission holography [29]. Only recently, Oelsner and Fecher proposed a new holographic scheme which involves the circular dichroism in order to recover the phase information from an angle-scanned photoelectron diffraction experiment [30].

3. Near-node photoelectron holography

Near-node photoelectron holography is an optimized form of inside-source holography [10,18]. The concept of near-node photoelectron holography is based on the anisotropic nature of photoelectron source waves and minimizes forward and multiple scattering. At electron kinetic energies above 500 eV, forward scattering is the strongest scattering feature in Auger electron and photoelectron diffraction. Forward scattering is a zero-order diffraction feature and has no holographic information. When forward scattering dominates, multiple scattering is most prominent along forward-scattering directions. Therefore the minimization of forward scattering minimizes multiple scattering as well [31]. In this section the basic idea of near-node photoelectron holography is reviewed. After theoretical considerations the first experimental confirmation of the validity of near-node photoelectron diffraction is reported.

3.1. Theory

The key quantity for the estimation of the importance of multiple scattering is the elastic mean free path $\lambda_e = 1/n\sigma_e$, where n is the atom density and σ_e the elastic scattering cross section that is calculated from the optical theorem:

$$\sigma_e = \frac{4\pi}{k} \Im f(\vartheta = 0). \tag{7}$$

$2\pi/k$ is the wavelength of the electrons and $\Im f(\vartheta = 0)$ is the imaginary part of the forward-scattering amplitude. From the optical theorem (equation (7)) and the de Broglie relation $k = \sqrt{2m_eE}/\hbar$, it is seen that the elastic mean free path scales with $\sqrt{E}$ and is inversely proportional to the forward-scattering amplitude. E is the kinetic energy and m_e the mass of the electron. In aluminium we thus get for electrons with a kinetic energy of 1 keV an elastic mean free path λ_e of 14 Å or five nearest-neighbour distances. From this relatively large number it follows that multiple scattering should not strongly interfere with the holographic reconstructions as long as molecular objects with a size $<\lambda_e$ are investigated. The forward scattering is, however, ubiquitous for any emitter below the top layer and produces artifacts in holographic reconstructions from the very first coordination shell, i.e. very close to the emitter. From equations (A.3) and (A.5) in the appendix it is seen that a forward-scattering peak with a width of 20°, for example, produces artifacts in the image function for $r > 0.7$ Å.

At first glance, forward scattering seems to be an intrinsic feature of photoelectron diffraction, at least if the emitter does not lie in the top layer. There is, however, a way around this problem if the anisotropic nature of the photoelectron source wave is exploited [10]. In a single-scattering picture, the photoelectron diffraction intensity $I(\boldsymbol{k})$ (equation (1)) may be written as

$$I(\boldsymbol{k}) = |\Psi_{source}(\vartheta \equiv 0, \boldsymbol{R}) + \sum_i \frac{f(\vartheta_i)}{|\boldsymbol{R} - \boldsymbol{r}_i|} \Psi_{source}(\vartheta_i, \boldsymbol{r}_i)|^2 \tag{8}$$

where the emitter (source) sits at the origin, $\boldsymbol{R}$ is the position of the detector (in the direction of $\boldsymbol{k}$) and $\boldsymbol{r}_i$ is the location of the scatterer (object) i. $f(\vartheta_i)$ is the complex scattering amplitude and ϑ_i is the angle between $\boldsymbol{r}_i$ and $\boldsymbol{R}$. $\Psi_{source}(\vartheta \equiv 0, \boldsymbol{R}) = \mathcal{A}(\vartheta = 0)/R$ is the reference wave Ψ_r with the arbitrary phase zero and an intensity $\propto \mathcal{A}^2$. $\Psi_{source}(\vartheta_i, \boldsymbol{r}_i) = (\mathcal{A}(\vartheta_i, \varphi_i)/r_i) \exp(\mathrm{i}r_i k\ (1 - \cos\vartheta_i))$ contains the phase factor $\exp(\mathrm{i}r_i k\ (1 - \cos\vartheta_i))$ with the holographic information. Accordingly, the importance of forward scattering, $\vartheta_i = 0$, scales with the intensity $\mathcal{A}^2$ of the reference wave. Therefore the Fraunhofer condition $|\Psi_r| \gg |\Psi_o|$ can generally not be optimized in electron holography since it would cause strong forward scattering. If the source wave is isotropic, i.e. $\mathcal{A}(\vartheta, \varphi) =$ constant, the relative weight of the forward scattering is constant. For anisotropic source waves, such as a p wave that is created by the photoexcitation of an s level, the relative importance of the reference wave and thus the weight of forward scattering can be tuned. From the considerations in section 2 it is furthermore seen that the photoexcitation of an s level with a defined light polarization $\boldsymbol{A}$ is the best choice for a source wave in photoelectron holography, since then the diffraction pattern is constituted by a single source wave, i.e. $Y_{1,m}$.

In figure 6, simulated XPD single-scattering patterns from a C 1s excited CO molecule are shown as a function of the angle γ between the plane of polarization and the detector. The forward scattering along the CO axis decreases $\propto \cos^2\gamma$ and the relative weight of the interference features passes a maximum near the node. If e.g. the electron emission direction lies on a node of the photoemission source wave, *no* forward scattering is expected. However, within the single-scattering picture, such photoelectron diffraction patterns cannot be considered as holograms, since the reference wave is missing in this geometry. For 1 keV

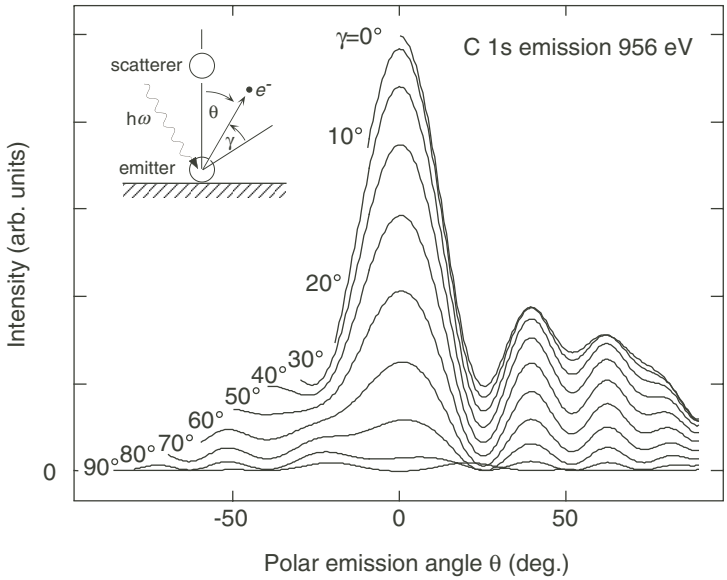

Figure 6. Theoretical C 1s (956 eV) x-ray photoelectron diffraction patterns from a CO molecule as depicted in the inset. For small angles γ between the direction of the x-rays and the electron detector, the forward scattering dominates, while for angles near the node (close to 90°), the interference fringes are most prominent. Data from reference [18].

electrons it was shown by scattering calculations that there is an optimum angle of about 10° ($\gamma = 80°$) near the nodal plane of an outgoing p wave, where the holographic reconstructions are best [10]. This angle is a compromise between the effect of the disturbing object self-interference term $\Psi_o \Psi_o^\star$ and that of the forward and multiple scattering. In figure 7, the *far-node* geometry is compared with the *near-node* geometry. The figure shows simulated photoelectron diffraction patterns and the corresponding holographic reconstructions for a single emitter and a single scatterer. In the near-node geometry, the relative weight of the interference pattern is strongly enhanced compared to that for the forward scattering. The holographic reconstruction from the diffraction pattern in the far-node geometry shows 'fingers' that correspond to the forward-scattering cone in the photoelectron diffraction near field. On the other hand, the diffraction data in the near-node geometry show 'droplet' features near the atomic site of the scatterer and its twin image. It has to be noted that near-node photoelectron holography requires a constant angle γ between the detector and the light polarization. Otherwise the near-node condition is not fulfilled for all emission directions. Therefore, in experiments of this kind, the sample has to be rotated with respect to the reference frame of the light source and the detector.

3.2. Experiments

The first near-node photoelectron holography experiments were performed on an Al(111) surface [37]. The face-centred cubic (fcc) structure of aluminium with a nearest-neighbour distance of 2.86 Å is known and the inversion symmetry of the fcc structure causes the twin image to coincide with the image. With a photon energy of 1070 eV the Al 2s electron wavelength becomes 0.4 Å. Two orientations of the linear light polarization were used. In the near-node geometry the angle γ between the detector and the polarization was set to 80° and

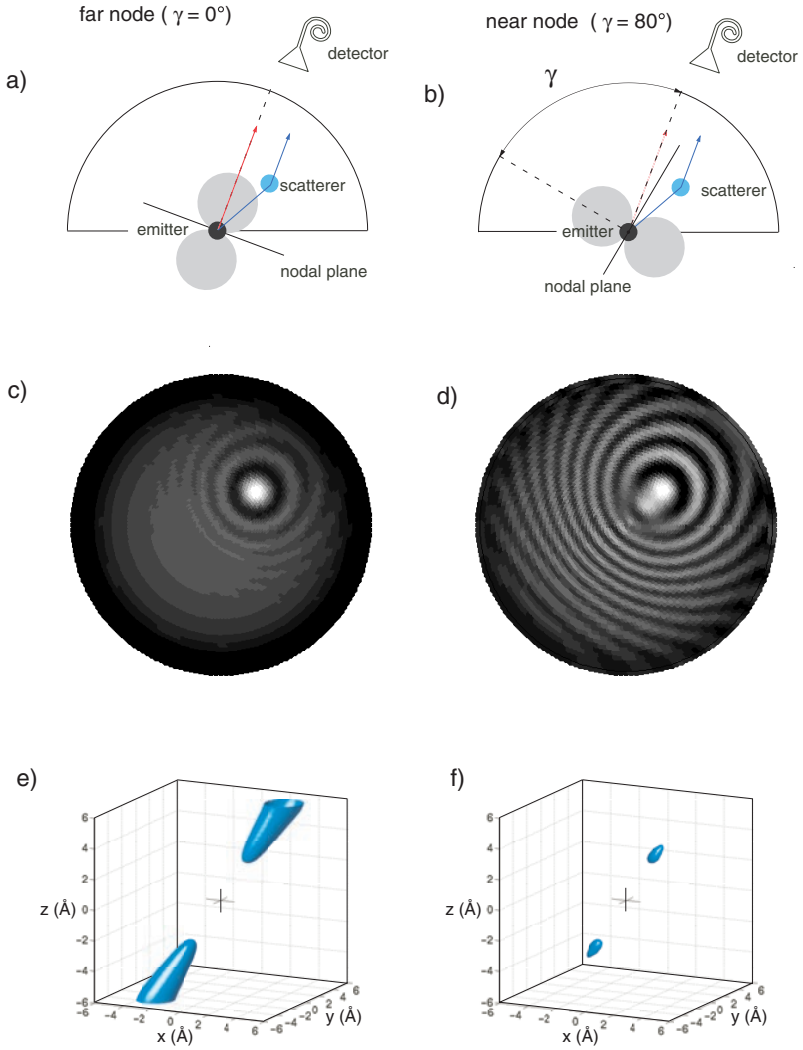

Figure 7. Photoelectron holography for the far- and near-node geometries. γ is the angle between the light polarization and the electron detector. Two configurations of a p source wave are indicated in (a) for the far-node geometry ($\gamma = 0^\circ$) and in (b) for the near-node geometry ($\gamma = 80^\circ$). The Al 2s emitter (inside source) ($\lambda = 0.4$ Å) is 2.86 Å away from the Al scatterer. The diffraction patterns in (c) and (d) are simulated with single-scattering calculations: they show the photoelectron diffraction intensity stereographically projected into the hemisphere above the surface with γ kept constant. In (c) the forward scattering along the emitter scatterer axis (bright spot) clearly dominates. In (d) the higher-order diffraction fringes are strongly enhanced compared to those for the forward scattering. In (e) and (f) the corresponding holographic reconstructions $|\boldsymbol{r}U(\boldsymbol{r})|^2$ are shown in three-dimensional isointensity representation. While the reconstruction from far-node diffraction shows 'finger'-like forward-scattering cones, the near-node reconstruction indicates the atomic site at $\boldsymbol{r}$ and its twin at $-\boldsymbol{r}$. From reference [38].

in the far-node geometry it was set to 0°. The far-node-geometry data served for comparison and the absolute determination of the crystal orientation. In order to remove the polar angle dependence of the instrumental response function, the azimuthal data sets (figures 8(a) and 8(c)) are normalized for every polar emission angle.

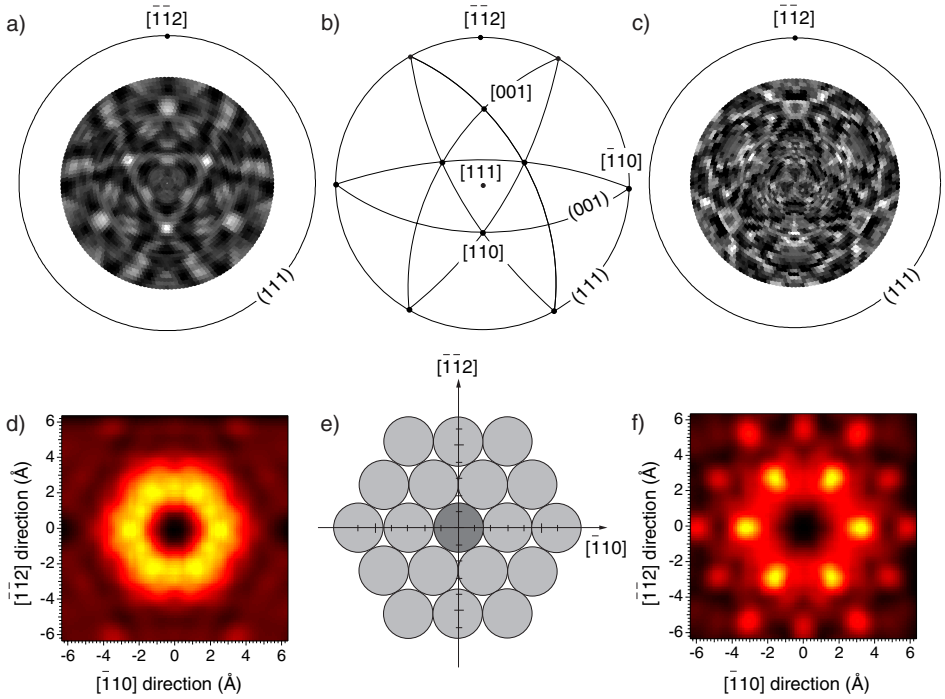

Figure 8. Comparison of far-node and near-node photoelectron diffraction data and their holographic reconstructions. (a), (c) Stereographically projected experimental Al 2s (E_{kin} = 942 eV) photoelectron diffraction patterns from an Al(111) single crystal for the far-node and the near-node geometry. In the far-node geometry (a), forward scattering dominates the pattern as can be seen from the stereographic projection of the high-density crystal chains and planes in (b). In the near-node diffraction pattern (hologram), no distinct forward-scattering features are visible. (d), (f) Corresponding holographic real-space reconstructions of a plane parallel to the surface that contains the emitter (inside source) at (0, 0). They should show the expected image of an Al(111) plane (e). In the near-node reconstruction (f) nearest, next-nearest and second-nearest neighbours are clearly resolved as local maxima, while in the far-node picture (d) no clear atom positions can be seen. From reference [37].

The angle-dependent Al 2s photoemission intensities for the far-node and the near-node geometry are stereographically projected in figures 8(a) and 8(c). White corresponds to the highest and black the lowest intensity. From comparison with figure 8(b) which shows the corresponding real-space projection of a fcc crystal onto the (111) plane, it is seen that the far-node diffraction pattern can be regarded as a projection of nuclear charge along the nearest-neighbour directions. The forward scattering focuses intensity along nearest-neighbour directions and thus causes high intensity along low-index atomic chains and planes [17]. This correspondence is not seen in the near-node diffraction pattern (figure 8(c)) and thus indicates suppression of forward scattering. From the diffraction patterns, real-space images of the emitter's environment were produced with the Stuck algorithm [36] (see the appendix). Care was taken by considering an apodizing function that smooths the edges of the diffraction patterns. This avoids unwanted high-frequency components, i.e. artifacts in the Fourier transform. The image function $|\boldsymbol{r}U(\boldsymbol{r})|^2$ is shown after a convolution with a Gaussian with 1 Å full width at half-maximum, without any low-intensity cut-off. In the near-node geometry, the holographic reconstruction of real space around the emitter in the (111) plane clearly reveals the positions of the surrounding atoms. In figure 8(f) nearest-, next-nearest- and even

second-nearest-neighbour positions are resolved as local maxima in the image. This is not the case for the far-node geometry data, where instead of distinct atomic positions a 'nearest-neighbour belt' is found. As usual with inside-source holography, the emitter sits at the origin of the image and is not reproduced.

In figure 9, three-dimensional images of the holographic reconstructions of the data in figures 8(a) and 8(c) are displayed [37]. The convoluted image functions are shown within a sphere around the emitter with 8 Å diameter. Intensities greater than 80% of the maximum intensity are displayed as opaque. Here it becomes even more obvious that the far-node diffraction data do not produce three-dimensional pictures of atomic sites. In order to compensate for the truncation of the nearest-neighbour shells in the top layers, the image function has been multiplied by a factor of $\exp(|z|/\Lambda)$ where $|z|$ is the distance from the emitter plane normal to the surface and Λ is the inelastic mean free path. From the data in figure 8(c) the three-dimensional structure of the twelve nearest neighbours around the emitter is recovered. In figure 9(b), the expected ABC stacking of subsequent (111) planes in the fcc structure is correctly reproduced. The holographic image is, however, not very precise as regards the *absolute* length. This is caused by the atomic scattering phase shifts that imply larger and anisotropic 'effective' scattering paths. All nearest-neighbour distances in figure 9(b) are overestimated by about one wavelength, but in a fairly isotropic way. The twelve emitter–nearest-neighbour distances scatter by 0.1 Å around the mean value of 3.4 Å (instead of 2.86 Å as expected from the fcc structure of aluminium). In summary, figures 8(f) and 9(b) indicate that the near-node photoelectron holography resolves in this case 24 different atomic positions without applying any correction schemes. There have also been experiments performed with a second photoelectron energy which resolved the first coordination shell as well, at the correct atomic positions [31].

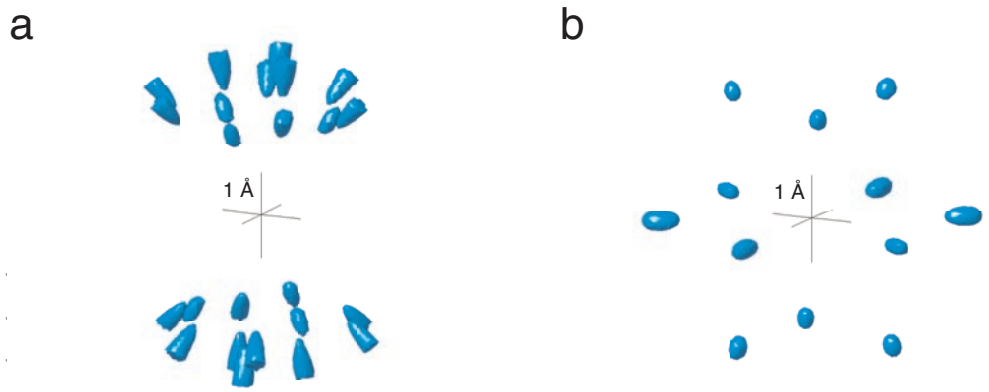

Figure 9. Three-dimensional isointensity representations of the holographic image as reconstructed from the photoelectron diffraction data in figures 8(a) and 8(c). The atomic environment of an Al 2s photoemitter at (0, 0, 0) in Al(111) is shown inside a shell with 4 Å radius. (a) Reconstruction from the standard geometry data (figure 8(a)) that indicates forward-scattering cones. (b) Reconstruction of the near-node photoelectron diffraction data which reproduces the expected atomic positions. From reference [39].

These findings demonstrate that the atomic structure of molecular objects with a size of the order of 10 Å can be explored with near-node photoelectron holography. The chemical sensitivity of core-level photoemission and the exploitation of the anisotropy of its source wave present an opportunity for structure determination in large unit cells with complicated molecular structures.

Acknowledgments

It is a great pleasure to thank Jürg Osterwalder and Joachim Wider for fruitful discussions and constant support. Financial support from the Swiss National Science Foundation is gratefully acknowledged.

Appendix. Inverting the data with the Stuck algorithm

In the following, a short summary of Stuck's solution of the Helmholtz–Kirchhoff theorem for the holographic inversion of full hemispherical 2π-scans is given [33, 34, 36]. The procedure is based on the multipole expansion as known e.g. from classical electrodynamics [40].

A1. Multipole expansion of 2π photoelectron diffraction data

It is convenient to expand an intensity distribution $I(\theta, \phi)$ as it is measured in a full hemispherical photoelectron diffraction experiment (see figure 1) into its multipole expansion coefficients $a_{\ell m}$ [40]:

$$I(\theta, \phi) = \sum_{\ell=0}^{\ell_{max}} \sum_{m=-\ell}^{\ell} a_{\ell m} Y_{\ell m}(\theta, \phi) \tag{A.1}$$

where $Y_{\ell m}$ are the normalized spherical harmonics (e.g. $Y_{11} = \sqrt{3/8\pi}\sin(\theta)\exp(\mathrm{i}\phi)$ or $Y_{00} = 1/\sqrt{4\pi}$). The multipole coefficients $a_{\ell m}$ are found from the integrals

$$a_{\ell m} = \int_{4\pi} I(\theta, \phi) Y^*_{\ell m}(\theta, \phi)\, \mathrm{d}\Omega. \tag{A.2}$$

Since $I(\theta, \phi)$ is real we have to calculate the integral (A.2) for $m \geqslant 0$ only. The coefficients $a_{\ell m}$ for negative m are given by $a_{\ell -m} = (-1)^m a^*_{\ell m}$. In our problem, $I(\theta, \phi)$ is known for the hemisphere above the surface $0 \leqslant \theta < \pi/2$. If we assume point symmetry, i.e. set for the hemisphere below the surface $I(\theta, \phi) = I(\pi - \theta, \pi + \phi)$, equation (A.2) has to be solved for even ℓ only, since $Y_{\ell m}(\theta, \phi) = (-1)^\ell Y_{\ell m}(\pi - \theta, \pi + \phi)$. For a given cut-off ℓ_{max} in the multipole expansion (equation (A.1)), the symmetry of the problem reduces the calculational effort from $(\ell_{max} + 1)^2$ over 4π to $2(\ell_{max}/2 + 1)^2$ over 2π or by roughly a factor of 4. The cut-off ℓ_{max} is given by the sampling density of $I(\theta, \phi)$ and the angular resolution. The solid angle of a cone with a full-width opening angle $\Delta\vartheta$ of 1° fills e.g. the hemisphere 26 000 times where for small $\Delta\vartheta$ the sampling density goes as $\Delta\vartheta^{-2}$. The sampling theorem of discrete Fourier transforms and the azimuthal factors $\exp(\mathrm{i}m\phi)$ of the $Y_{\ell m}$ give an upper limit ℓ_{max}:

$$\ell_{max} \leqslant \frac{\pi}{\Delta\vartheta}. \tag{A.3}$$

In figure A1 the amplitudes of the multipole expansion coefficients of the Cu 3s ($E_{kin} =$ 1365 eV) photoelectron diffraction data from a Cu(110) surface are shown in an m versus ℓ diagram. It can be seen that the twofold rotational symmetry of the diffraction pattern is reflected in the large contribution of the twofold-symmetric $Y_{\ell m}$ where m is even. As is demonstrated in figure A2, the $a_{\ell m}$ may be used for an efficient filtering and for the subtraction of the instrumental response function which is a function of the emission angle θ. The response function is a smooth, Gaussian-like function and is constituted by coefficients $a_{\ell 0}$ with small ℓ. In figure A2(b) the data from figure A2(a) are shown for the multipole expansion with an ℓ_{max} of 60. This greatly reduces the noise in the data. In figure A2(c), $a_{0,0}, a_{2,0}, \ldots, a_{12,0}$ are set to zero, which removes the instrumental response function.

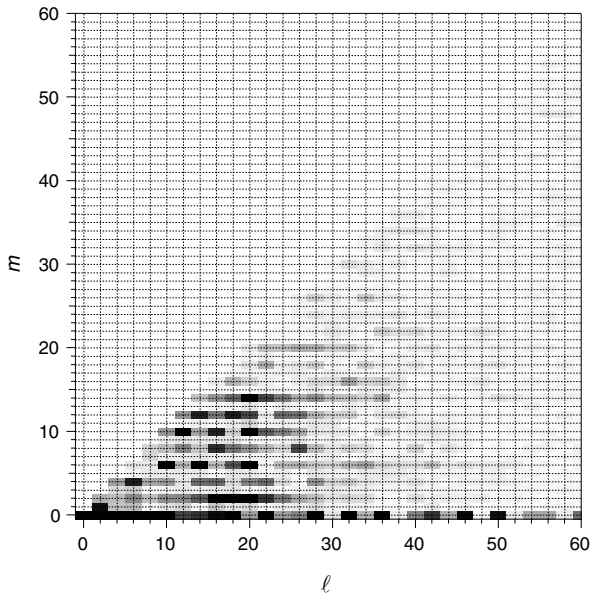

Figure A1. Multipole expansion coefficients $a_{\ell m}$ of the 2π-scan in figure A2(a). The amplitudes of the $a_{\ell m}$ are displayed on a truncated linear greyscale where white corresponds to $a_{\ell m} = 0$ and black to values $|a_{\ell m}| \geqslant 3 \times 10^{-3} a_{00}$. Note: only coefficients $a_{\ell m}$ with even ℓ and $0 \leqslant m \leqslant \ell$ are calculated and displayed. The dominance of the $a_{\ell m}$ with even m indicates the twofold rotational symmetry of the Cu(110) 2π-scan in figure A2(a).

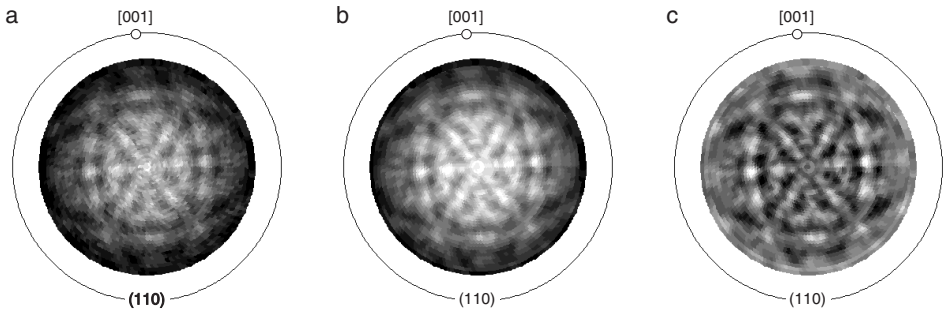

Figure A2. Filtering effects of different multipole coefficients. (a) Raw data from a Cu 3s $E_{kin} = 1365$ eV 2π-scan of Cu(110). (b) $I(\theta, \phi)$ from the coefficients $a_{\ell m}$ with $\ell \leqslant 60$. (c) After removal of an 'instrumental response function', setting $a_{\ell 0} = 0\ \forall \ell \leqslant 12$. From [41].

A2. The Fourier transform

As was shown by Stuck *et al* the multipole expansion (equation (A.1)) is a perfect starting point for the reconstruction of the photoelectron near field from the measured far field [36]. The scalar wave field $U(\boldsymbol{r})$ in the vicinity of the emitter is

$$U(\boldsymbol{r}) \propto \sum_{\ell=1}^{\ell_{max}} (\mathrm{i})^{-\ell} j_\ell(kr) \sum_{m=-\ell}^{\ell} a_{\ell m} Y_{\ell m}(\alpha, \beta) \tag{A.4}$$

where $j_\ell(kr)$ are the spherical Bessel functions ($j_0(x) = \sin(x)/x$), k is the electron wave vector and $Y_{\ell m}$ are the spherical harmonics. Here r, α and β are the spherical coordinates, i.e. the magnitude, the polar and azimuthal angles of $\boldsymbol{r}$ with respect to the emitter. Equation (A.4) is the Fourier transform of $I(\theta, \phi)$ (see equation (A.1)). It can also be considered as the reconstruction of the wave field using Huygens' principle [36]. Note that the first sum in equation (A.4) runs from $\ell = 1$ only, which is equivalent to the holographic inversion of the conventionally used image function $\chi \propto I(\theta, \phi) - I_0$ where I_0 is the average intensity. From the known coefficients $a_{\ell m}$ and equation (A.4), the holographic image function $|\boldsymbol{r}U(\boldsymbol{r})|^2$ may be calculated. $U(\boldsymbol{r})$ is multiplied by $\boldsymbol{r}$ in order to get an image intensity which is independent of $|\boldsymbol{r}|$. The function $|\boldsymbol{r}U(\boldsymbol{r})|^2$ is large at atomic positions (scattering centres) and has strong $\sin^2(kr)$ modulations from the Bessel functions. These modulations are removed by a convenient convolution with a full width at half-maximum $>\lambda$.

It is instructive to discuss the function $U(\boldsymbol{r}) = U(z)$ along the surface normal ($\alpha = 0$). Equation (A.4) simplifies to

$$U(z) \propto \sum_{\ell=1}^{\ell_{max}} \sqrt{(2\ell+1)} a_{\ell 0} (\mathrm{i})^{-\ell} j_\ell(kz).$$

We see that the $m \neq 0$ components do not contribute to $U(z)$, since for these spherical harmonics $\int_{2\pi} Y_{\ell m}(\theta, \phi)\, \mathrm{d}\phi$ vanishes [34,36]. This important result is equivalent to the finding of Saldin *et al* [42], who pointed out that the distance r of a scatterer may be found by Fourier transformation of the azimuthally averaged intensity around the direction of $\boldsymbol{r}$. Of course, this statement must be valid for an arbitrary direction ($\alpha \neq 0, \beta$) of $\boldsymbol{r}$, but then, the new coefficients $a'_{\ell 0}(\alpha, \beta)$ have to be calculated from the $a_{\ell m}(\theta\phi)$.

Using the multipole expansion formalism, the issue of 'reach' and angular resolution for angle-scanned photoelectron holography may be discussed. The spherical Bessel functions make their strongest contribution to the image at $kr \approx 2 + \ell$ [40]. From this, it is directly seen that the coefficients $a_{\ell m}$ with small ℓ contribute to the image in the vicinity of the emitter and those with large ℓ to the image far away. Thus, ℓ_{max} limits the 'reach' R_{max} of photoelectron holography to

$$R_{max} \sim \frac{2 + \ell_{max}}{k} \tag{A.5}$$

and with this and equation (A.3) we find for 1000 eV photoelectrons and an angular resolution $\Delta\vartheta$ of 2° that

$$R_{max} \approx \frac{\pi}{\Delta\vartheta\, k} \approx 6\ \text{Å}.$$

References

[1] Osterwalder J, Greber T, Stuck A and Schlapbach L 1991 *Phys. Rev.* B **44** 13 764
[2] Baird R J, Fadley C S and Wagner L F 1977 *Phys. Rev.* B **15** 666
[3] Owari M, Kudo M, Nikei Y and Kamada H 1985 *Japan. J. Appl. Phys.* **24** L394
[4] Li H and Tonner B P 1988 *Phys. Rev.* B **37** 3959
[5] Frank D G, Battina N, Golden R, Lu F and Hubbard A T 1990 *Science* **247** 182
[6] Seelmann-Eggebert M and Richter H J 1991 *Phys. Rev.* B **43** 9578
[7] Wider J, Greber T, Wetli E, Kreutz T J, Schwaller P and Osterwalder J 1998 *Surf. Sci.* **414** 301
[8] Harp G R, Saldin D K and Tonner B P 1990 *Phys. Rev.* B **42** 9199
[9] Gabor D 1948 *Nature* **161** 777
[10] Greber T and Osterwalder J 1996 *Chem. Phys. Lett.* **256** 653
[11] Szöke A 1986 *Short Wavelength Coherent Radiation: Generation and Applications (AIP Conf. Proc. No 147)* ed D T Attwood and J Boker (New York: American Institute of Physics) pp 361–467
[12] Barton J J 1988 *Phys. Rev. Lett.* **61** 1356

[13] Barton J J 1991 *Phys. Rev. Lett.* **67** 3106
[14] Tegze M, Faigel G, Marchesini S, Belakhovsky M and Chumakov A I 1999 *Phys. Rev. Lett.* **82** 4847
[15] Korecki P, Korecki J and Ślezak T 1997 *Phys. Rev. Lett.* **79** 3518
[16] Wu H, Lapeyre G J, Huang H and Tong S Y 1993 *Phys. Rev. Lett.* **71** 251
[17] Fadley C S 1993 *Surf. Sci. Rep.* **19** 231
[18] Greber T and Osterwalder J 1996 *Prog. Surf. Sci.* **53** 163
[19] Greber T, Osterwalder J, Hüfner S and Schlapbach L 1992 *Phys. Rev.* B **45** 4540
[20] Goldberg S M, Fadley C S and Kono S 1981 *J. Electron Spectrosc. Relat. Phenom.* **21** 285
[21] Jackson G J, Cowie B C C, Woodruff D P, Jones R G, Kariapper M S, Fisher C, Chan A S Y and Butterfield M 2000 *Phys. Rev. Lett.* **84** 2346
[22] Yeh J J and Lindau I 1985 *At. Data Nucl. Data Tables* **32** 1
[23] Idzerda Y U and Ramaker D E 1992 *Phys. Rev. Lett.* **69** 1943
[24] Greber T, Osterwalder J, Naumović D, Stuck A, Hüfner S and Schlapbach L 1992 *Phys. Rev. Lett.* **69** 1947
[25] Sincović B, Orders P J, Fadley C S, Trehan R, Hussain Z and Lecante J 1984 *Phys. Rev.* B **30** 1833
[26] Daimon H, Nakanti T, Imada S, Suga S, Kagoshima Y and Myahara T 1993 *Japan. J. Appl. Phys.* **32** L1480
[27] Daimon H 2001 *Phys. Rev. Lett.* **86** 2035
[28] Sambi M and Granozzi G 1998 *Surf. Sci.* **415** L1007
[29] Li H and Tong S Y 1993 *Surf. Sci.* **282** 380
[30] Oelsner A and Fecher G H 1999 *J. Electron Spectrosc. Relat. Phenom.* **101–103** 455
[31] Wider J 2001 *Dissertation* University of Zürich
[32] Tonner B P, Han Z-L, Harp G R and Saldin D K 1991 *Phys. Rev.* B **42** 14 423
[33] Stuck A, Naumović D, Greber T, Osterwalder J and Schlapbach L 1992 *Surf. Sci.* **274** 441
[34] Osterwalder J, Fasel R, Stuck A, Aebi P and Schlapbach L 1994 *J. Electron. Spectrosc. Relat. Phenom.* **68** 1
[35] Tong S Y, Huang H and Wei C M 1992 *Phys. Rev.* B **46** 2452
[36] Stuck A, Naumović D, Aebischer H A, Greber T, Osterwalder J and Schlapbach L 1992 *Surf. Sci.* **264** 380
[37] Wider J, Baumberger F, Sambi M, Gotter R, Verdini A, Bruno F, Cvetko D, Morgante A, Greber T and Osterwalder J 2001 *Phys. Rev. Lett.* **86** 2337
[38] Greber T, Wider J, Verdini A, Morgante A and Osterwalder J 2001 *Eur. Phys. News* **32** 172
[39] Wider J and Greber T 2001 *Neue Zürcher Zeitung* **112** 75
[40] Jackson J D 1975 *Classical Electrodynamics* 2nd edn (New York: Wiley)
[41] Wider J 2001 unpublished
[42] Saldin D K, Harp G R, Chen B L and Tonner B P 1991 *Phys. Rev.* B **44** 2480